metals

MDPI

Article

Microstructure Characteristics and Corrosion Behaviors of Mg-2Zn-2Er-0.3Zr-0.3Mn Alloy under Various Rolling Reductions

Yaqi Zheng, Yuan Zhang *,†, Yun Liu, Yaqiang Tian, Xiaoping Zheng and Liansheng Chen *,†

Key Laboratory of the Ministry of Education for Modern Metallurgy Technology, College of Metallurgy and Energy, North China University of Science and Technology, Tangshan 063210, China; zyqnb1991@163.com (Y.Z.); liuyun@ncst.edu.cn (Y.L.); tyqwylfive@163.com (Y.T.); zhengxp1978@163.com (X.Z.)

* Correspondence: zhangy130481@ncst.edu.cn (Y.Z.); kyckfk@ncst.edu.cn (L.C.); Tel.: +86-0315-8805420 (Y.Z.); +86-0315-8805420 (L.C.)

† These authors contributed equally to this work.

Abstract: The poor corrosion resistance of magnesium alloys is one of the major obstacles to their widespread applications in the engineering field and the medical field. A hot deformation process is the main way to improve the corrosion resistance of magnesium alloys. In the present study, X-ray photoelectron spectroscopy (XPS), a scanning electron microscope (SEM), an electron probe micro-analyzer (EPMA) and X-ray diffraction (XRD) were used to investigate the micro-galvanic corrosion behavior and film protection mechanism of hot-rolled Mg-2Zn-2Er-0.3Zr-0.3Mn under 25%, 50% and 75% thickness reductions in Hank's solution. The results revealed that the best corrosion resistance was obtained in the alloy under a 75% thickness reduction, with a corrosion rate of 0.85 mm/y. The improvement in anti-corrosion was due to the coupling effect of a refined microstructure and dense degradation film on the large deformation hot-rolled alloy. Furthermore, the elements Mn and Er participated in the film formation and stabilized the film structure.

Keywords: degradation film; refined microstructure; micro-galvanic corrosion; various rolling reduction

check for updates

Citation: Zheng, Y.; Zhang, Y.; Liu, Y.; Tian, Y.; Zheng, X.; Chen, L. Microstructure Characteristics and Corrosion Behaviors of Mg-2Zn-2Er-0.3Zr-0.3Mn Alloy under Various Rolling Reductions. *Metals* **2022**, *12*, 365. https://doi.org/10.3390/met12020365

Academic Editor: Sebastian Feliu Batlle

Received: 5 January 2022
Accepted: 16 February 2022
Published: 21 February 2022

Publisher's Note: MDPI stays neutral with regard to jurisdictional claims in published maps and institutional affiliations.

Copyright: © 2022 by the authors. Licensee MDPI, Basel, Switzerland. This article is an open access article distributed under the terms and conditions of the Creative Commons Attribution (CC BY) license (https://creativecommons.org/licenses/by/4.0/).

1. Introduction

Mg-based alloys have been regarded as excellent biomedical materials and achieve complete degradation due to a low density, good progressing ability and specific elastic modulus, which is similar to natural bone [1,2]. Nonetheless, in an electrolyte environment with a large number of corrosive ions (Cl^-, HPO_4^{2-}, CO_3^{2-}, etc.), mechanical integrity may be lost prematurely, even causing tissue necrosis [3–5]. A low absolute strength and relatively low corrosion resistance are two main disadvantages that restrict wide industrial and clinical applications of Mg alloys. They are essential to improving the corrosion resistance by alloying elements and performing the deformation process of magnesium alloys for their successful application as bearing structures and implant materials.

The element Er has not been extensively studied to enhance the anti-corrosion ability, while the mechanical property has been significantly improved by using Er [6–9]. For decades, the corrosion behaviors of Mg-RE-Zn-based alloys containing $Mg_{12}YZn$, which have long-period stacking-ordered (LPSO) and $(Mg, Zn)_3Gd$ phases, have been reported [10–14]. A refined microstructure and compact layers can enhance the corrosion resistance by reducing the micro-galvanic intensity, facilitating the reaction kinetics of film formation and stabilizing the film layer [15–20]. Panemangalore et al. [21] found that the corrosion resistance of Mg-2Zn was greatly enhanced by the addition of the element Er (2 wt.%). The corrosion rate decreased from 0.13 to 0.078 mm/y.

Moreover, thermal deformation processes, such as extrusion and rolling, are regarded as effective ways to modify the corrosion resistances of magnesium alloys. Rolling, a

significant manufacturing technology for Mg strips or plates, has the advantages of high efficiency and flexibility among all thermal mechanical processes. It can modify the corrosion behavior of Mg alloys by using a refined grain size, reduced segregation and redistributed precipitates. Koleini et al. [22] stated that the hot-rolled process remarkably reduced the high-corrosion tendency of an as-cast Mg-1Ca alloy in an SBF (simulated body fluid) solution. Xiang et al. [23] reported that a current density reduced from $9.5 \pm 1.2 \times 10^{-4}$ to $2.5 \pm 2.0 \times 10^{-4}$ A/cm^2 by using the hot-rolled process. Furthermore, Estrin et al. [24] reported that a Mg-4Li-1Ca alloy, processed by using two-step rolling, showed superiority in bone implants. Bakhsheshi-Rad et al. [25] stated that the corrosion resistance is related to the secondary phase. However, corrosion occurs preferentially at the interface between the LPSO phase and the Mg matrix. The 18R-LPSO phase combines well with the matrix and also keeps a high corrosion resistance. Thus, the corrosion resistance of a Mg-Zn-Y-Er alloy can be improved. These opinions provide a new perspective for developing Mg-Zn-Er alloys. Moreover, the elements Er and Mn are considered to be beneficial to the corrosion behavior of Mg alloys [26,27].

Until now, little research has referred to the corrosion behavior of Mg-Er alloys. In this study, a Mg-2Zn-2Er-0.3Mn-0.3Zr (wt.%) (MZEZM) alloy was used to study the influence of hot rolling on the corrosion resistance of MZEZM. Weight loss tests, electrochemical tests and corrosion morphology observations were systematically performed to evaluate the corrosion rate with different processing conditions in Hank's solution. Finally, the degradation mechanism, by using the synergistic effect of the refined-grain structure and the stability of the corrosion film, was revealed.

2. Materials and Methods

2.1. Materials Fabrication

Mg-2Zn-2Er-0.3Zr-0.3Mn was prepared by using an electric resistance furnace (MRL-8, Huizhou Tianji Magnesium Industry Co., Ltd., Guangdong, China). The alloy elements Zn, Er, Mn and Zr were added by melting pure zinc (99.9% purity), Mg-30Zr (99.9% purity), Mg-10Mn (99.9% purity) and Mg-20Er (99.9% purity) master alloys. To ensure proper alloying, the master alloys were melted at 750 °C for 20 min under a protective gas of N2 and SF6 with a volume ratio of 6:1. Then, the molten alloy was poured into graphite molds with zinc oxide coatings. The as-cast samples were annealed at 350 °C for 12 h and cooled down in air. The total reductions in thickness were 25 (2 steps), 50 (5 steps) and 75% (9 steps), named HR-25, HR-50 and HR-75, respectively. Between each two-rolling step, samples were reheated to 350 °C for 10 min. The deformation of each pass was less than 15%, which was intended to avoid cracking.

2.2. Microstructure Characteristics

Test specimens were mechanically ground on silicon carbide sand paper (#160, #400, #800, #1500, #2500 and #3000) in sequence, then polished and etched with a mixed solution of 4 g picric acid, 3.6 mL glacial acetic acid, 70 mL absolute ethanol and 16.4 mL deionized (DI) water. The corrosion product was removed by using a 200 g/L CrO_3 and 10 g/L $AgNO_3$ solution for 60 s and then was weighted with analytical balances. The microstructures were revealed by using optical microscopy (OM, DM6M, Leica, Brackenheim, Germany), a scanning electron microscope (SEM, Scios, FEI Company, Brno, Czech Republic) and an electron probe micro-analyzer (EPMA, JXA-8230, Rigaku Corporation, Yamanashi, Japan), which was equipped with a back-scattered electron imaging mode. Phase analyses were performed with an X-ray diffractometer (XRD, D/MAX2500PC, JEOL, Tokyo, Japan) with CuK_α radiation at a scanning speed of 10°/min.

2.3. Weight Loss Test

The samples for electrochemical tests were ground on SiC papers of up to 2500 grit and then washed thoroughly with distilled water and dried by using cold air. For weight loss testing in Hank's solution, each sample with a cross-section of about 10 mm (RD:

rolling direction) × 10 mm (TD: transverse direction) and a thickness of about 1.5 mm was immersed for 7 days at 37 °C. After the immersion test, the corroded specimens were carefully cleaned with a solution consisting of 200 g/L of CrO_3 and 10 g/L of $AgNO_3$ at 100 °C, and then the mass changes were measured with a precision balance. The corrosion rate (mm/y) was calculated by using the following equation [28]:

$$CR = 8.67 \times 10^4 \times \Delta W/(A \cdot T \cdot D) \quad (1)$$

where Δw was the weight loss after the immersion test, g; A was the surface area of the samples, cm^2; T was the period of the immersion test, hours and D was the density of the sample, $g \cdot cm^{-3}$.

2.4. Electrochemical Testing

All the electrochemical measurements were performed at an electrochemical work station (CORRTEST CS2350, Wuhan, China) with a conventional three-electrode system in Hank's solution, incorporated with a saturated calomel electrode (SCE), a Pt counter electrode and a working electrode (testing materials). Electrochemical measurements were conducted on samples with an area of 1 cm^2. The samples were immersed in Hank's solution for 15 min to obtain a relatively stable open-circuit potential (E_{OCP}). Then, the potentiodynamic polarization was set with a scan rate of 1 mV and a scan range from −0.6 V to 0.6 V (relative to E_{OCP}). Three samples were tested for each electrochemical to reduce errors. The Tafel extrapolation method was used to fit polarization curves using the software CView (Version 3.5d, Scribner Associates, Inc., Southern Pines, NC, USA). In Equation (2), the corrosion rate P_i (mm/y) could be calculated by using the corrosion current density, i_{corr} ($\mu A/cm^2$) [28]:

$$P_i = 22.85\ i_{corr} \quad (2)$$

Furthermore, the corrosion resistance of the sample was evaluated by using electrochemical impedance spectroscopy (EIS) measurements in Hank's solution at a body temperature of 37 °C. The EIS measurements were obtained (100 kHz~100 mHz) with an amplitude signal of 5 mV (E_{OCP}). The EIS data were fitted and analyzed by using the software Zsimpwin (Version 3.60, EChem Software, Ann Arbor, Michigan, USA). At least three samples were tested for each composition for the electrochemical measurements to ensure accuracy.

2.5. X-ray Photoelectron Spectroscopy

X-ray photoelectron spectroscopy (XPS, Thermo Scientific EACALAB Xi+, ThermoFisher, Waltham, MA, USA) measurements were performed on the films of corroded MZEZM alloys to analyze the compositions of the corrosion products. The software Avantage (Version 5.948, Micro Focus Ltd., Newbury, UK) was used to fit the XPS data. A C_{1s} peak (284.6 eV) was used to correct the binding energy scale.

3. Results

3.1. Microstructural Characterization

Figure 1 shows the OM microstructures of the as-cast and hot-rolled (HR) samples. For the HR samples, the horizontal direction was the hot-rolled direction. At the deformation of 25%, a large number of lamellar twins appeared in the Mg matrix, accompanied by the phenomenon of a twin–twin intersection in the original grains. The dynamic recrystallization (DRX) nucleation began to occur at the twin–twin intersection (Figure 1b). With the increase in the deformation, the fraction of DRX increased. A large number of equiaxed grains existed in the HR-50 and HR-75 alloys due to the large deformation process. Figure 2 shows EPMA images of the HR-75 alloy, which represent the α-Mg grains, secondary phases and element distributions. An EPMA analysis was carried out in order to further analyze the distributions of the other micro-alloying elements in the alloys. Figure 2 shows

the element maps of Mg, Zn and Er. The elements Zn and Er are obviously enriched in the secondary phases, which are located at the grain boundary. During the hot-rolled progress, the secondary phases were broken.

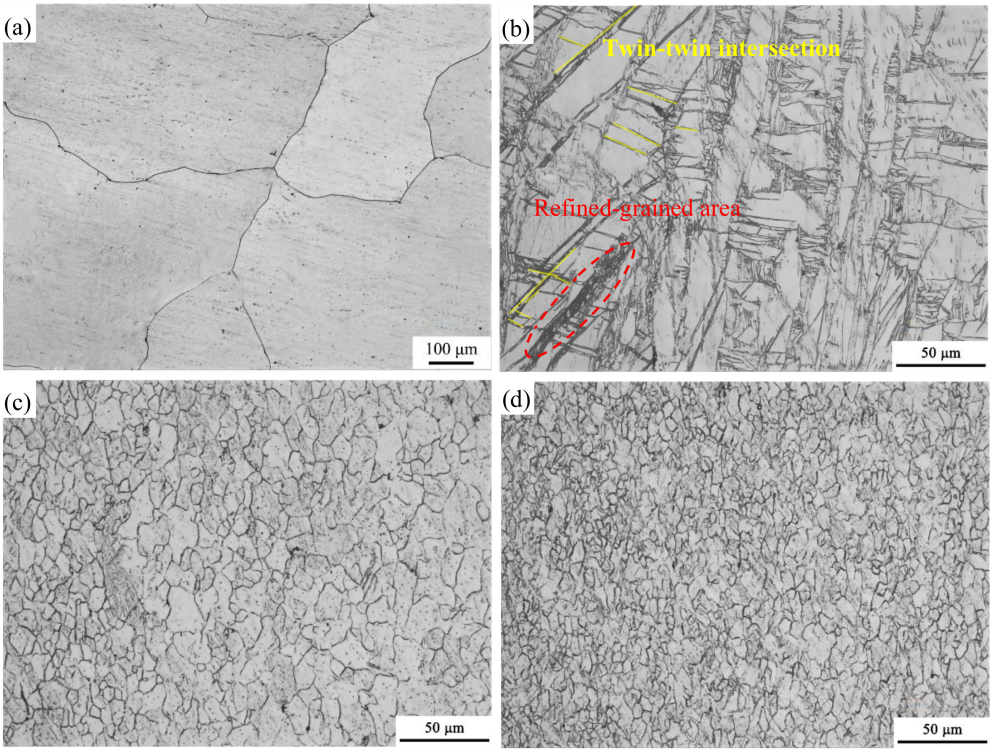


Figure 1. (**a**–**d**) Optical micrographs of as-cast, HR-25, HR-50 and HR-75 samples.

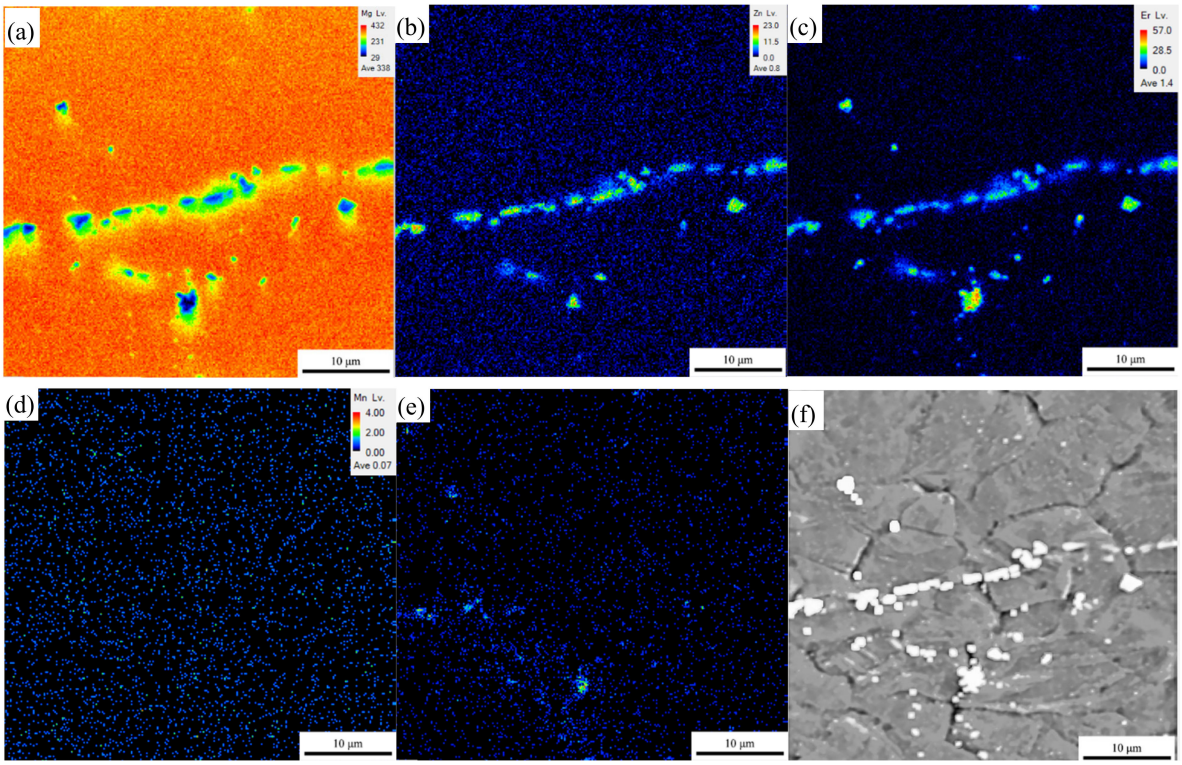


Figure 2. EPMA analysis of secondary phase distributions of HR-75 alloy (**a**) Mg element, (**b**) Zn element, (**c**) Er element, (**d**) Mn element, (**e**) Zr element and (**f**) microstructure of the secondary phase.

Figure 3 shows the XRD patterns of the Mg-2Zn-2Er-0.3Zr-0.3Mn as-cast and hot-rolled alloys, respectively. In the picture, the diffraction peaks of the W phase (face-centered cubic phase, $Mg_3Zn_3Er_2$) and α-Mg are observed. A small Mg-Zn binary phase was detected in the as-cast and HR samples. Moreover, with the hot-rolled process, the α-Mg (0002) and ($2\bar{1}\bar{1}2$) peak of the sample shifted to a higher angle, which indicated that the basal texture increased during the deformation process. A reflection of lattice distortion was caused by macroscopic residual stress.

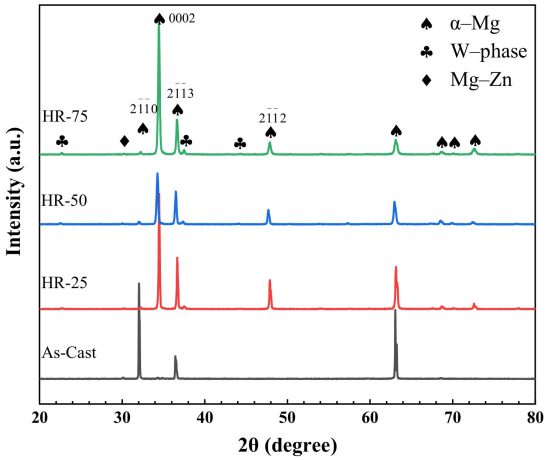


Figure 3. XRD pattern of the as-cast and hot-rolled alloys.

3.2. Corrosion Behavior of MZEZM Alloy in Hank's Solution

Weight Loss Test

The weight loss rates of the four samples after immersion in Hank's solution for 7 days was measured, and the responsible data are listed in Table 1. The weight loss rates of the as-cast and HR-25 samples were larger than those of the other two samples during the immersion test, implying that the as-cast and HR-25 alloys suffered more corrosion damage. It should be mentioned that the corrosion rates of the HR-25, HR-50 and HR-75 alloys decreased in turn by 1.72, 1.08 and 0.85 mm/y, respectively.

Table 1. Corrosion rates of four samples.

Sample	Corrosion Rate (mm y^{-1})
As-cast	1.13
HR-25	1.72
HR-50	1.08
HR-75	0.85

3.3. Corrosion Morphologies

3.3.1. The Morphologies and Qualities of Corrosion Products

Figure 4 shows the SEM images of the surface morphologies of the as-cast and hot-rolled alloys after immersion in Hank's solution for 7 days. The surfaces of all the alloys were covered by accumulated corrosion products. The quantities of corrosion production had increased in the order of HR-25, as-cast, HR-50 and HR-75, suggesting that the HR-75 alloy exhibited the best corrosion resistance. After a 7 day immersion test, a corrosion product layer with a micro-crack covered the surfaces of the HR-75 and HR-50 alloys, while a large number of white precipitation clusters dispersed on the surfaces of the other two samples (Figure 4e). Corrosion products in the shape of needle-like clusters are a typical morphology of brucite [$Mg(OH)_2$] [29], which grows perpendicular to the surface. The XRD data presented in Figure 4g proves that the corrosion products were mainly composed of $Mg(OH)_2$, HA (hydroxyapatite) and $MgCO_3$.

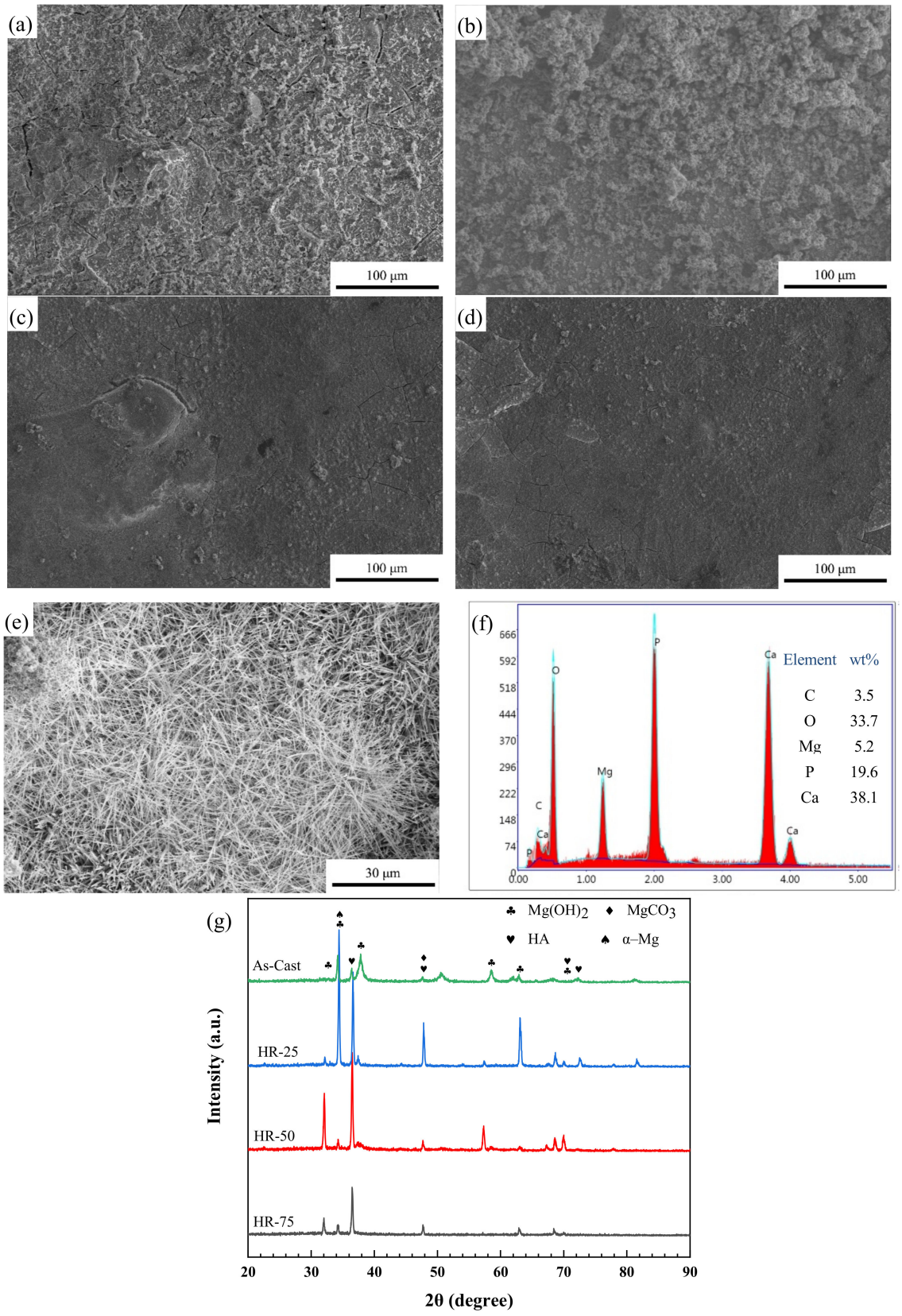


Figure 4. (**a**–**d**) Surface morphologies of as-cast, HR-25, HR-50 and HR-75 alloys after immersion in Hank's solution for 7 days, (**e**) enlarged image of the corrosion film, (**f**) EDS of the corrosion product and (**g**) XRD patterns of the films of four alloys.

3.3.2. Corrosion Morphology Analysis

After the immersion in Hank's solution for 7 days, severe localized corrosion was found on the as-cast and HR-25 samples; in contrast, the HR-50 and HR-75 samples revealed uniform corrosion and filiform corrosion. The corrosion films shown in Figure 4a,b reflect that the films were rugged and sparse, which improved the possibility of corrosion ions contacting the substrate. A large number of corrosion pits and gullies, which can be found in Figure 5a,b, improved the ions' ability to pass through the channel in the sparse corrosion film and produce a strong galvanic corrosion reaction with the substrate. On the contrast, the films of the HR-50 and HR-75 samples were dense and smooth, which was implied by the characteristics of filiform and uniform corrosion (Figure 5c,d).

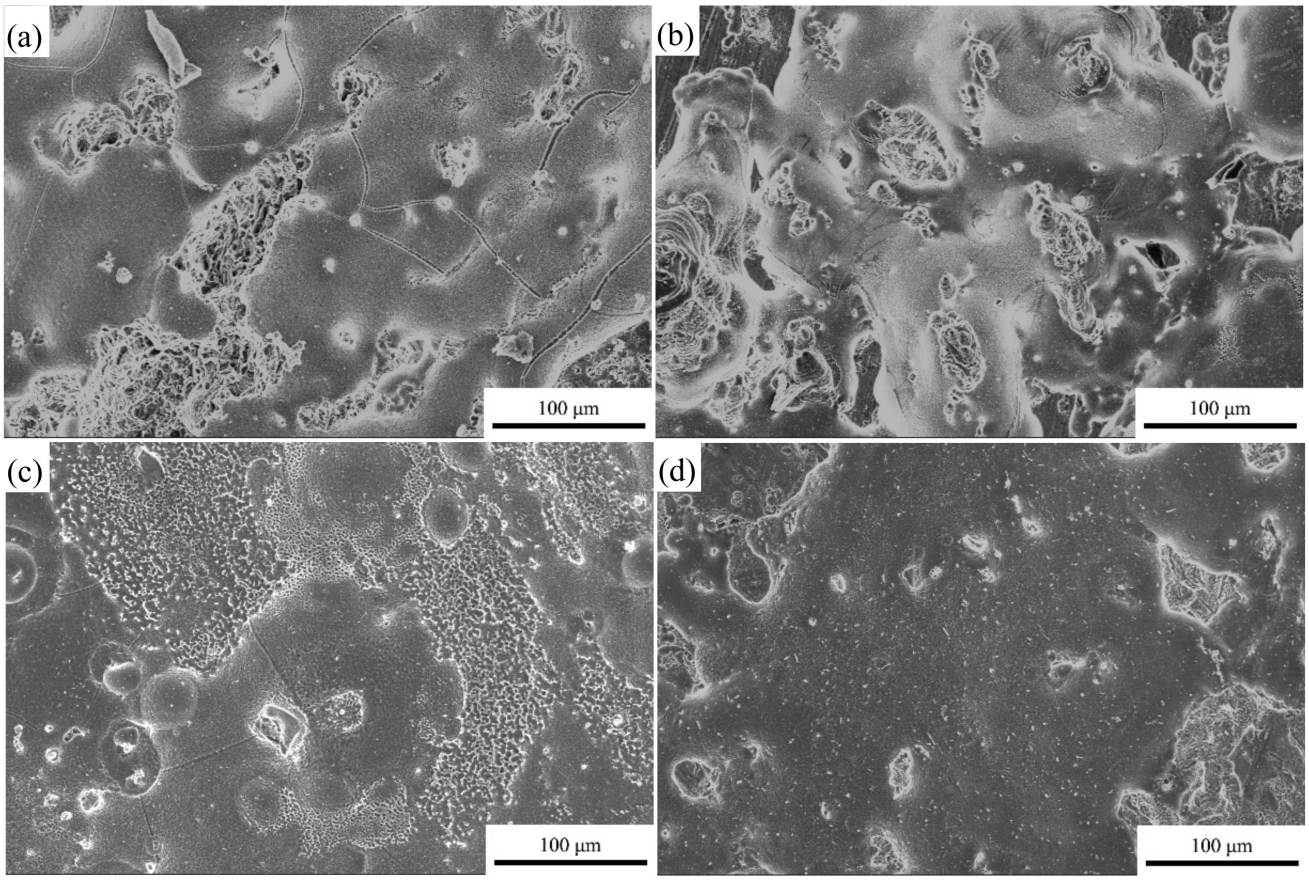


Figure 5. Corroded surface morphologies of the (**a**) as-cast alloy, (**b**) HR-25 alloy, (**c**) HR-50 alloy and (**d**) HR-75 alloy after immersion in Hank's solution for 7 days.

3.3.3. Polarization Tests

The polarization curves of the as-cast and HR samples after their immersion in an electrolyte for 500 s are shown in Figure 6. The values of corrosion potential (E_{corr}) and the corrosion current densities (i_{corr}) extracted from the polarization curves are illustrated in Table 2. The βc represents cathodic slopes. The values of i_{corr} increased with the increase in the rolling reduction. The polarization curves of the as-cast, HR-50 and HR-75 samples had similar characteristics, and a breakdown potential (E_{pt}) appeared near the potential of −1.3 V, which indicated that a temporary protective oxide film was formed on the surface of the sample. A breakdown potential did not exist in the HR-25 alloy. The HR-25 sample had the largest i_{corr}. The corrosion rate decreased in the following order: HR-25 > as-cast > HR-50 > HR-75; it showed the same tendency with the weight loss test.

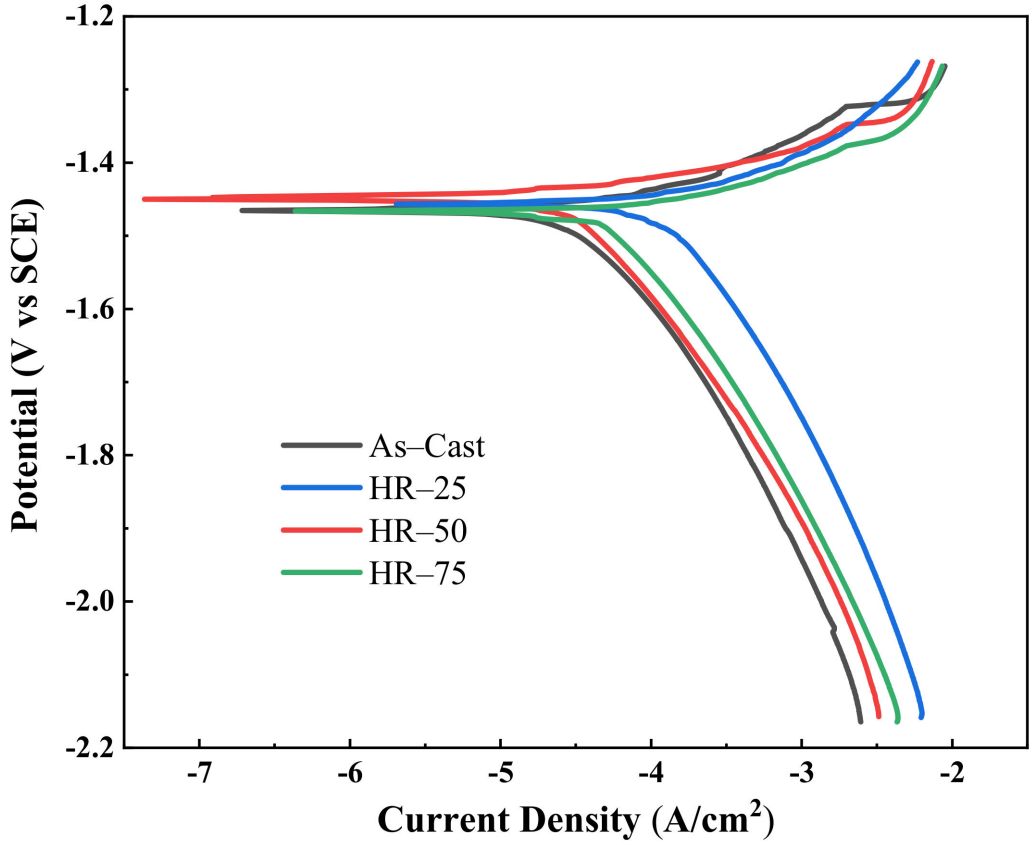


Figure 6. Polarization tests of the as-cast and HR alloys in Hank's solution.

Table 2. Polarization-curve fitting results.

State	E_{corr} (V_{SCE})	β_c	i_{corr} (μA/cm^2)	Corrosion Rate (mm/y)
As-Cast	−1.47	−2.64	57.15	1.31
HR-25	−1.46	−2.91	125.89	2.88
HR-50	−1.44	−3.02	44.16	1.01
HR-75	−1.46	−3.40	37.41	0.85

3.3.4. Electrochemical Impedance Spectroscopy (EIS)

Nyquist curves were plotted from the EIS measurement in Hank's solution (Figure 7) to further reveal the evolution of degradation behavior during immersion. An equivalent electrical circuit is shown in Figure 7 to fit the EIS data. The EIS of the as-cast, HR-25 and HR-50 samples contained a capacitance loop (high frequency), a capacitance loop (medium frequency) and an inductance loop (low frequency). The inductance loop of HR-75 was small. R_s represented the solution resistance, while the layer resistance (R_f) paralleled with a constant phase element (CPE_f), which was related to the oxidized layer. R_{ct} represented the charge transfer resistance related to the dissolution. Moreover, the double layer capacitance in parallel with R_{ct} was represented by CPE_{dl} with the inductance L, which represented the occurrence of a localized corrosion or micro-galvanic event. The comparison of EIS plots proved that there was a better protection ability of the film of HR-75 formed in Hank's solution than the others.

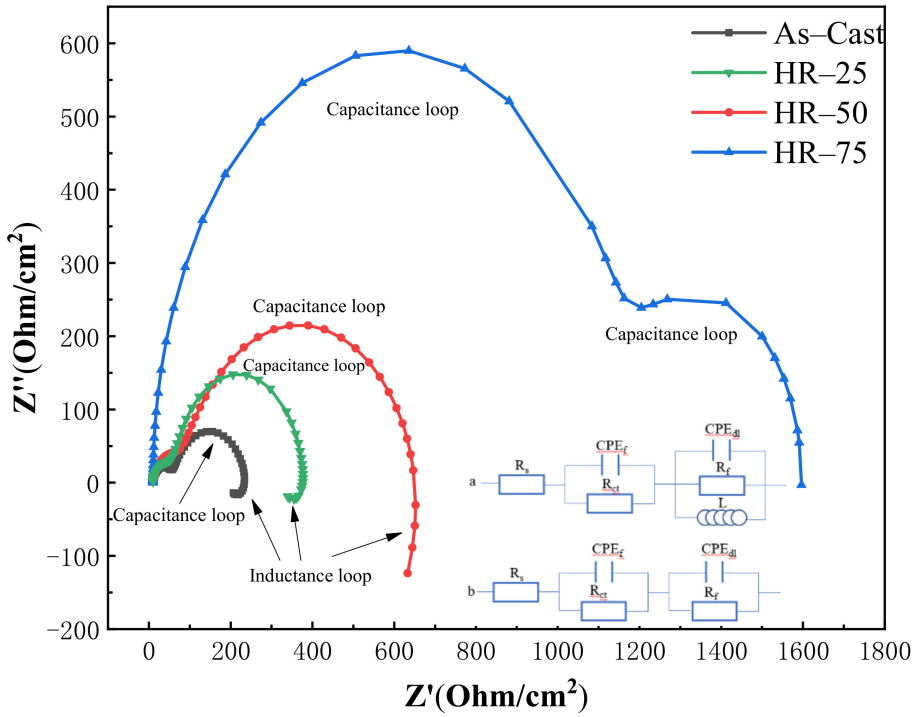


Figure 7. Nyquist plot and equivalent circuits.

3.3.5. XPS

To obtain more information about the possible corrosive product, XPS spectra for Mn_{2p} and Er in Hank's solution were measured and plotted in Figure 8. As displayed in the XRD diffraction in Figure 4g, $Mg(OH)_2$, HA and $MgCO_3$ were enriched in the outer layers of the corrosion products, hinting that the Mg, C, O and P elements precipitated to form the corrosion products during the degradation in Hank's solution. Nevertheless, according to the XPS survey spectrum in Figure 8, Mn and Er were detected in the corrosion layer. However, the signal of Er_{4d} was low and noisy, confirming the existence of a small amount of the element Er in the corrosion layer.

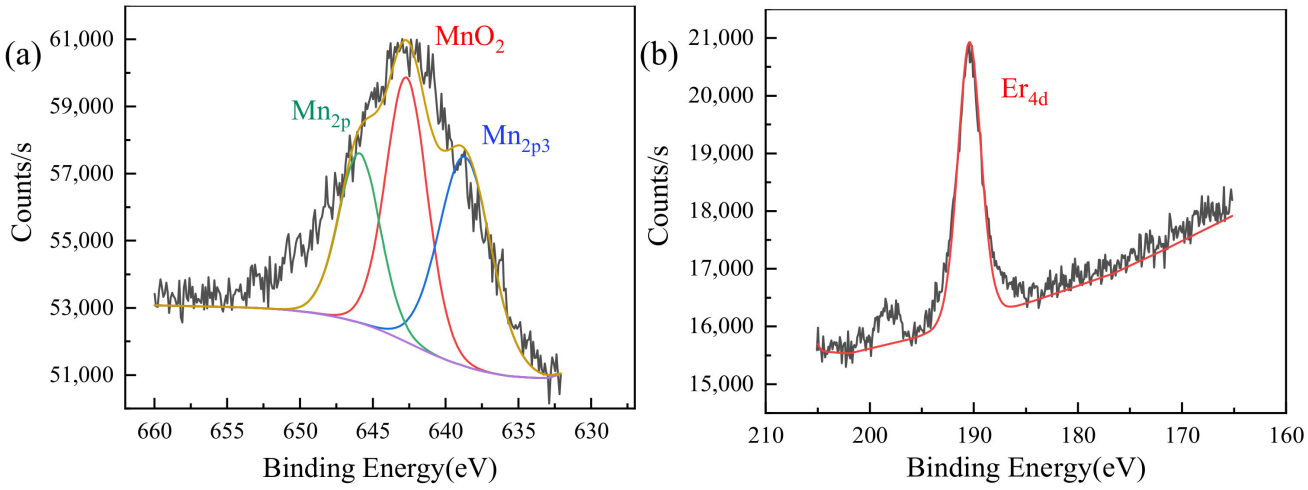


Figure 8. XPS analysis of the corrosion products formed on the HR-75 alloy: (**a**) Mn_{2p} spectrum (**b**) and Er_{4d} spectrum.

4. Discussion

According to the electrochemical results, the film morphology and the immersion analysis, there was a significant improvement in the corrosion resistance of the hot-rolled

MZEZM alloy with a large deformation. The results showed that the refined microstructure was beneficial for ameliorating the corrosion activity. The percentage of grain boundaries became greater with the smaller grains. Since the activities of the grain boundaries were different from those of the cores, a large number of the grain boundaries could achieve uniform corrosion. Another factor influencing the corrosion activity of the MZEZM alloy was twins. A large amount of deformation twins was observed in the microstructure of HR-25. The deformation twins increased the galvanic corrosion; therefore, HR-25 showed the fastest dissolution rate.

4.1. Microstructure of MZEZM

The as-cast MZEZM had coarser grains with a grain size of about 600 μm, while the HR-50 and HR-75 alloys had more refined grain microstructures of about 8 and 6 μm, approximately 1/75 and 1/100 of the original grain sizes. The HR-25 alloy contained a large number of twins surrounded by small grains. The dynamic recrystallization during the hot-rolled process promoted the grain refinement.

The element Er exhibited a good solubility in Mg at a high temperature. With the decrease in temperature, a $Mg_3Zn_3Er_2$ phase was observed in the grains and on the boundaries (Figure 2). The element Er also refined the microstructure effectively and reduced the mismatch stress between the α-Mg matrix and the surface, which could decrease the pitting initiation [30]. The controlled addition of Zr and Zn could suppress the adverse effects of the harmful impurities (Fe, Cu, Ni) on corrosion resistance [31,32]. The element Zr could also refine grain size by provide heterogenous nucleation sites. Mn is a common alloying element in Mg alloys because it refines the microstructures of Mg-Zn, Mg-Zn-RE, etc. by using PSN (particle stimulated nucleation). The inhibition effect of the Mn element on the growth of DRX is strong during the elastic deformation process [33]. Moreover, a Mn oxide film acts as a barrier against Cl ion penetration and improves the corrosion properties.

4.2. Comparison of Corrosion Resistances of As-Cast and Hot-Rolled MZEZM Alloys in Hank's Solution

The corrosion rate values from the immersion in Hank's solution highlighted the difference between the as-cast and hot-rolled MZEZM alloys (Table 1). The as-cast sample exhibited a larger corrosion rate than the HR-50 and HR-75 samples, while HR-25 showed the highest corrosion rate. Since a large number of twins were produced during the deformation (which can decrease the electrochemical potential of a Mg substrate and increase the anodic dissolution, as shown in Figure 1b), there was a strong micro-galvanic event between the secondary phases and the matrix [34]. After the 7 day immersion test, it was possible to observe small particles, which stacked on the surface (Figure 4b) and were identified as $Mg(OH)_2$ and $MgCO_3$ (Figure 4g) [35,36]. The non-uniform roughened surface showed that the intense hydrogen evolution caused the constant and heterogeneous spalling of the corrosion products from the surface. The intensities of the peaks of corrosion products (Figure 4g), such as $Mg(OH)_2$ and $MgCO_3$, did not follow a certain rule, probably due to the spalling of the oxidation corrosion products. Figure 8 shows that the elements Mn and Er participated in the formation of a corrosion film. Although the element Mn stabilized the film structure [37,38], the severe hydrogen evolution effect had a stronger damage effect on the film layer.

This study confirmed that a large thickness-reduction hot-rolled process can enhance the corrosion resistance of an MZEZM alloy by producing a uniform structure, fine grains and a stable corrosion film. An oxide film can easily form when an MZEZM alloy immerses in Hank's solution. An active dissolution occurs during the immersion test. Twins and impurities, such as Fe, Ni and Cu, act as cathodes, which are more inter- than anode Mg, thus promoting the micro-galvanic corrosion (reaction (3)–(5)) [39,40]. Then, a porous magnesium hydroxide film is formed on the surface.

$$2H_2O + 2e^- \rightarrow 2OH^- + H_2\uparrow \quad (3)$$

$$Mg \rightarrow Mg^{2+} + 2e^{-} \quad (4)$$

$$Mg + 2H_2O \rightarrow Mg(OH)_2 + H_2\uparrow \quad (5)$$

Figure 6 shows the potentiodynamic polarization measurement of the immersion in Hank's solution. The corrosion rates from large to small are HR-25, as-cast, HR-50 and HR-75. The current density plateaus on the anodic curves of as-cast, HR-50 and HR-75 were observed and attributed to the protective corrosion film on the surface. On the contrary, the current density of HR-25 increased monotonously. This was consistent with the formation of non-protective properties. This indicated that the twins destroyed the uniformity and integrity of the film. Due to the large deformation, the defects in the matrix were greatly reduced, and HR-75 showed a uniformly corroded surface with the best corrosion resistance.

To further reveal the evolution of corrosion behavior during immersion, Nyquist plots were obtained from the EIS measurement in Hank's solution (Figure 7). The XRDs of HR-25 and HR-50 indicated larger amounts of corrosion products than HR-75 due to the violent hydrogen-evolution reaction. The reaction produced a loose and porous corrosion film and promoted a continuous reaction between the matrix and corrosion ions. The subsequent reactions produced more corrosion products. The dense and flat corrosion film of HR-75 acted as a physical barrier to slow down local corrosion initiation and expansion. This was consistent with EIS and polarization curves. HR-75 had the largest R_{ct}, which indicated that the refined grains could obtain a corrosion film with a good compactness and integrity. In addition, HR-75 showed a small attendance of pitting corrosion, which corresponded to the unobvious low frequency inductance curves. An inductance loop in the low frequency region could be observed from the other three loops (Figure 7), indicating the breakdown of reaction layers. Table 3 shows that the solution resistances (R_s) of the four samples were approximately same, around 10 $\Omega \cdot cm^2$. The charge transfer resistances (R_{ct}) and resistances of the films (R_f) determined the corrosion resistances of the alloys. According to the diameter of the loop and fitting parameters, the degradation rates of the samples were HR-25, as-cast, HR-50 and HR-75, in increasing order. Moreover, a larger diameter of the semicircle in the Nyquist plot represented a more superior corrosion protective property [41]. The HR-75 plot showed a much more superior impedance at any frequency than the other three plots. The almost invisible low frequency inductance loop meant that the corrosion film was relatively complete and prevented the local corrosion [42]. The film resistances of HR-50 and HR-75 were much larger than those of as-cast and HR-25 (Table 3). The comparison of EIS plots proved that the films of as-cast and HR-25 contained weak protection abilities. Moreover, the large R_{ct} of HR-50 and HR-75 indicated that the kinetics of Mg dissolution and hydrogen gas evolution were slower than in the as-cast and HR-25 alloys due to the protection of the uniform and dense films. In addition, HR-75 showed an excellent corrosion resistance compared to the corrosion behaviors of the other hot-rolled alloys (Table 4).

Table 3. Fitting results of the EIS spectra.

Sample	R_s ($\Omega \cdot cm^2$)	CPE_f ($\mu\Omega^{-1} \cdot cm^{-2} \cdot s^n$)	n_1	R_{ct} ($\Omega \cdot cm^{-2}$)	CPE_{dl} ($\mu\Omega^{-1} \cdot cm^{-2} \cdot s^n$)	n_2	R_f ($\Omega \cdot cm^2$)	L ($H \cdot cm^2$)
As-cast	10.57	196	0.80	192.7	4.78	0.89	44.27	37.73
25%	9.80	27.61	0.93	327.5	5.85	0.88	48.2	31.41
50%	11.68	2.67	0.92	60.28	44.0	0.80	597.20	1062
75%	10.08	1.8	0.98	1145	1185	0.90	401.6	-

Table 4. Comparison of corrosion rates of hot-rolled Mg alloys in literature and this work.

Alloy	Solution	Corrosion Rate (mm/y)	Reference
HR-75	Hank's	0.85	This work
Mg-1.5Sn-0.5Ca	0.35 wt.%NaCl	4.31	[43]
Mg-1.5Sn-0.5Ca-0.1Ce	0.35 wt.%NaCl	3.12	[43]
AZ31	0.5 M NaCl	10.3	[44]
Mg-8Sn-1Al-1Zn	0.6 M NaCl	19	[45]
Mg-2Zn-0.2Mn-0.62Nd	Kokubo	0.92	[15]
Mg-5Gd	3.5 wt.% NaCl	0.7	[46]
Mg-4Li-1Ca	SBF	12.3	[47]
Mg-4Li	SBF	104	[47]

5. Conclusions

In this study, Mg-2Zn-2Er-0.3Zr-0.3Mn alloys were prepared by using as-cast and hot-rolled processes. The microstructure and the corrosion behavior of Mg-2Zn-2Er-0.3Mn-0.3Zr in Hank's solution were systematically investigated. The HR-75 alloy showed a good corrosion resistance and had an excellent potential in the field of high-corrosion resistant Mg-alloy materials. Some conclusions were obtained:

1. The main phase composition included an α-Mg matrix, a W phase and a Mg-Zn phase. With the increase in the hot-rolled reduction, the degree of dispersion distribution of the secondary phase increased. The main factors influencing the corrosion resistance of Mg-Zn-Er-Mn-Zr were the grain size contribution and the film structure. The better long-term degradation performance of the alloy with a large deformation was due to the different structure of the oxide film and the secondary phase and due to the refined grains. The worst corrosion resistance of HR-25 was due to the generation of twins.
2. According to the results of the electrochemical test, the corrosion rates of the four samples were in the order of HR-25, as-cast, HR-50 and HR-75 with the corrosion rates of 2.88, 1.31, 1.01 and 0.85 mm/y, respectively. The reason for the abnormal corrosion rate of HR-25 was that the non-uniform grain-size distribution enhanced the hydrogen evolution effect, leading to the spalling of the oxidation corrosion products and resulting in the weak corrosion resistance of HR-25.
3. The reasons for the high corrosion resistance of HR-50 and HR-75 were that the fine-grain and homogeneous structure could reduce the hydrogen chemical kinetics, protect the integrity of the film and insulate the contact reaction between the erosive ions and the substrate.

Author Contributions: Formal analysis, Y.Z. (Yaqi Zheng) and Y.Z. (Yuan Zhang); resources, Y.T. and X.Z.; data curation, Y.Z. (Yaqi Zheng) and Y.Z. (Yuan Zhang); writing—original draft preparation, Y.Z. (Yaqi Zheng), Y.Z. (Yuan Zhang), Y.L. and L.C. All authors have read and agreed to the published version of the manuscript.

Funding: This research was funded by the Natural Science Foundation of Hebei Province (E2020209153); Natural Science Foundation—Steel and Iron Foundation of Hebei Province (E2020209124; E2020209127); Fundamental Research Funds for the Provincial Universities of Hebei (JYG2019001); State Key Lab of Advanced Metals and Materials (2020-Z12) and Science and Technology Project of Tangshan (20130205b).

Institutional Review Board Statement: Not applicable.

Informed Consent Statement: Not applicable.

Data Availability Statement: Not applicable.

Conflicts of Interest: The authors declare no conflict of interest.

References

1. Liu, J.N.; Bian, D.; Zheng, Y.F.; Chu, X.; Lin, Y.L.; Wang, M.; Lin, Z.F.; Li, M.; Zhang, Y.; Guan, S.K. Comparative in vitro study on binary Mg-RE (Sc, Y, La, Ce, Pr, Nd, Sm, Eu, Gd, Tb, Dy, Ho, Er, Tm, Yb and Lu) alloy systems. *Acta Biomater.* **2020**, *102*, 508–528. [CrossRef]
2. Zheng, M.B.; Xu, G.Q.; Liu, D.B.; Zhao, Y.; Ning, B.Q.; Chen, M.F. Study on the Microstructure, Mechanical Properties and Corrosion Behavior of Mg–Zn–Ca Alloy Wire for Biomaterial Application. *J. Mater. Eng. Perform.* **2018**, *27*, 1837–1846. [CrossRef]
3. Wen, Y.F.; Liu, Q.S.; Wang, J.F.; Yang, Q.M.; Zhao, W.K.; Qiao, B.; Li, Y.L.; Jiang, D.M. Improving in vitro and in vivo corrosion resistance and biocompatibility of Mg–1Zn–1Sn alloys by microalloying with Sr. *Bioact. Mater.* **2021**, *6*, 4654–4669. [CrossRef] [PubMed]
4. Lotfpour, M.; Dehghanian, C.; Emamy, M.; Bahmani, A.; Malekan, M.; Saadati, A.; Taghizadeh, M.; Shokouhimehr, M. In-vitro corrosion behavior of the cast and extruded biodegradable Mg-Zn-Cu alloys in simulated body fluid (SBF). *J. Magnes. Alloys* **2021**, *9*, 2078–2096. [CrossRef]
5. Liu, Y.C.; Liu, D.B.; Zhao, Y.; Chen, M.F. Corrosion degradation behavior of Mg–Ca alloy with high Ca content in SBF. *Trans. Nonferr. Met. Soc. China* **2015**, *25*, 3339–3347. [CrossRef]
6. Li, H.; Du, W.B.; Li, S.B.; Wang, Z.H. Effect of Zn/Er weight ratio on phase formation and mechanical properties of as-cast Mg–Zn–Er alloys. *Mater. Des.* **2012**, *35*, 259–265. [CrossRef]
7. Wang, Q.F.; Liu, K.; Wang, Z.H.; Li, S.B.; Du, W.B. Microstructure, texture and mechanical properties of as-extruded Mg–Zn–Er alloys containing W-phase. *J. Alloys Compd.* **2014**, *602*, 32–39. [CrossRef]
8. Pereira, G.S.; Koga, G.Y.; Avila, J.A.; Bittencourt, I.M.; Fernandez, F.; Miyazaki, M.H.; Botta, W.J.; Filho, W.W.B. Corrosion resistance of WE43 Mg alloy in sodium chloride solution. *Mater. Chem. Phys.* **2021**, *272*, 124930. [CrossRef]
9. Zhao, X.; Li, S.; Wang, Q.; Du, W.; Liu, K. Effects of heat treatment on microstructure and mechanical properties of Mg–5Zn–0.63Er alloy. *Trans. Nonferr. Met. Soc. China* **2013**, *23*, 59–65. [CrossRef]
10. Zengin, H.; Turen, Y. Effect of Y addition on microstructure and corrosion behavior of extruded Mg–Zn–Nd–Zr alloy. *J. Magnes. Alloys* **2020**, *8*, 640–653. [CrossRef]
11. Wu, L.Y.; Li, H.T. Effect of selective oxidation on corrosion behavior of Mg–Gd–Y–Zn–Zr alloy. *Corros. Sci.* **2018**, *142*, 238–248. [CrossRef]
12. Li, C.Q.; Xu, D.K.; Zeng, Z.R.; Wang, B.J.; Sheng, L.Y.; Chen, X.B.; Han, E.H. Effect of volume fraction of LPSO phases on corrosion and mechanical properties of Mg-Zn-Y alloys. *Mater. Des.* **2017**, *121*, 430–441. [CrossRef]
13. Zhang, J.S.; Xu, J.D.; Cheng, W.L.; Chen, C.J.; Kang, J.J. Corrosion Behavior of Mg–Zn–Y Alloy with Long-period Stacking Ordered Structures. *J. Mater. Sci. Technol.* **2012**, *28*, 1157–1162. [CrossRef]
14. Zhang, X.B.; Dai, J.W.; Zhang, R.F.; Ba, Z.X.; Birbilis, N. Corrosion behavior of Mg–3Gd–1Zn–0.4Zr alloy with and without stacking faults. *J. Magnes. Alloys* **2019**, *7*, 240–248. [CrossRef]
15. Zhang, Y.; Li, J.Y.; Liu, Y.; Chen, L.S. Microstructure characteristics, film layer rupture mechanism and corrosion behavior of hot-rolled Mg-2Zn-0.2Mn-xNd. *Mater. Charact.* **2020**, *165*, 110368. [CrossRef]
16. Wei, L.Y.; Li, J.Y.; Zhang, Y.; Lai, H.Y. Effects of Zn content on microstructure, mechanical and degradation behaviors of Mg-xZn-0.2Ca-0.1Mn alloys. *Mater. Chem. Phys.* **2020**, *241*, 122441. [CrossRef]
17. Zhang, Y.; Li, J.X.; Li, J.Y. Microstructure, mechanical properties, corrosion behavior and film formation mechanism of Mg-Zn-Mn-xNd in Kokubo's solution. *J. Alloys Compd.* **2018**, *730*, 458–470. [CrossRef]
18. Zhang, Y.; Li, J.Y.; Liaw, P.K.; Xu, Y.Z.; Lai, H.Y. Effects of heat treatment on the mechanical properties and corrosion behaviour of the Mg-2Zn-0.2Mn-xNd alloys. *J. Alloys Compd.* **2018**, *769*, 552–565. [CrossRef]
19. Li, J.X.; Zhang, Y.; Li, J.Y.; Xie, J.X. Effect of trace HA on microstructure, mechanical properties and corrosion behavior of Mg-2Zn-0.5Sr alloy. *J. Mater. Sci. Technol.* **2018**, *34*, 299–310. [CrossRef]
20. Cai, C.H.; Song, R.B.; Wen, E.D.; Wang, Y.J.; Li, J.Y. Effect of microstructure evolution on tensile fracture behavior of Mg-2Zn-1Nd-0.6Zr alloy for biomedical applications. *Mater. Des.* **2019**, *182*, 108038. [CrossRef]
21. Panemangalore, D.B.; Shabadi, R.; Gupta, M. Effect of fluoride coatings on the corrosion behavior of Mg-Zn-Er alloys. *Surf. Interfaces* **2019**, *14*, 72–81. [CrossRef]
22. Koleini, S.; Idris, M.H.; Jafari, H. Influence of hot rolling parameters on microstructure and biodegradability of Mg–1Ca alloy in simulated body fluid. *Mater. Des.* **2012**, *33*, 20–25. [CrossRef]
23. Xiang, Q.; Jiang, B.; Zhang, Y.X.; Chen, X.B.; Song, J.F.; Xu, J.Y.; Fang, L.; Pan, F.S. Effect of rolling-induced microstructure on corrosion behaviour of an as-extruded Mg-5Li-1Al alloy sheet. *Corros. Sci.* **2017**, *119*, 14–22. [CrossRef]
24. Estrin, Y.; Nene, S.S.; Kashyap, B.P.; Prabhu, N.; Al-Samman, T. New hot rolled Mg-4Li-1Ca alloy: A potential candidate for automotive and biodegradable implant applications. *Mater. Lett.* **2016**, *173*, 252–256. [CrossRef]
25. Bakhsheshi-Rad, H.R.; Abdul-Kadir, M.R.; Idris, M.H.; Farahany, S. Relationship between the corrosion behavior and the thermal characteristics and microstructure of Mg–0.5Ca–xZn alloys. *Corros. Sci.* **2012**, *64*, 184–197. [CrossRef]
26. Liu, Y.; Cheng, W.L.; Gu, X.J.; Liu, Y.H.; Cui, Z.Q.; Wang, L.F.; Wang, H.X. Tailoring the microstructural characteristic and improving the corrosion resistance of extruded dilute Mg–0.5Bi–0.5Sn alloy by microalloying with Mn. *J. Magnes. Alloys* **2020**, *9*, 1656–1668. [CrossRef]
27. Baek, S.M.; Lee, S.Y.; Kim, J.C.; Kwon, J.; Jung, H.; Lee, S.; Lee, K.S.; Park, S.S. Role of trace additions of Mn and Y in improving the corrosion resistance of Mg–3Al–1Zn alloy. *Corros. Sci.* **2021**, *178*, 108998. [CrossRef]

28. Gao, G.J.; Zeng, M.Q.; Zhang, E.L.; Zeng, R.C.; Cui, L.Y.; Xu, D.K.; Wang, F.Q.; Kannan, M.B. Dealloying corrosion of anodic and nanometric Mg41Nd5 in solid solution-treated Mg-3Nd-1Li-0.2Zn alloy. *J. Mater. Sci. Technol.* **2021**, *83*, 161–178. [CrossRef]
29. Feliu, S.; Llorente, I. Corrosion product layers on magnesium alloys AZ31 and AZ61: Surface chemistry and protective ability. *Appl. Surf. Sci.* **2015**, *347*, 736–746. [CrossRef]
30. Xie, J.S.; Zhang, J.H.; You, Z.H.; Liu, S.J.; Guan, K.; Wu, R.Z.; Wang, J.; Feng, J. Towards developing Mg alloys with simultaneously improved strength and corrosion resistance via RE alloying. *J. Magnes. Alloys* **2021**, *9*, 41–56. [CrossRef]
31. Zhou, Y.Y.; Fu, P.H.; Peng, L.M.; Wang, D.; Wang, Y.X.; Hu, B.; Liu, M.; Sachdev, A.K.; Ding, W.J. Precipitation modification in cast Mg–1Nd–1Ce–Zr alloy by Zn addition. *J. Magnes. Alloys* **2019**, *7*, 113–123. [CrossRef]
32. Wang, W.Z.; Wu, D.; Chen, R.S.; Qi, Y.; Ye, H.Q.; Yang, Z.Q. Revisiting the role of Zr micro-alloying in a Mg-Nd-Zn alloy. *J. Alloys Compd.* **2020**, *832*, 155016. [CrossRef]
33. Wang, J.F.; Lu, R.P.; Qin, D.Z.; Huang, X.F.; Pan, F.S. A study of the ultrahigh damping capacities in Mg–Mn alloys. *Mater. Sci. Eng. A* **2013**, *560*, 667–671. [CrossRef]
34. Hamu, G.B.; Eliezer, D.; Wagner, L. The relation between severe plastic deformation microstructure and corrosion behavior of AZ31 magnesium alloy. *J. Alloys Compd.* **2009**, *468*, 222–229. [CrossRef]
35. Yang, L.; Zhang, E.L. Biocorrosion behavior of magnesium alloy in different simulated fluids for biomedical application. *Mater. Sci. Eng. C* **2009**, *29*, 1691–1696. [CrossRef]
36. Johnston, S.; Shi, Z.M.; Atrens, A. The influence of pH on the corrosion rate of high-purity Mg, AZ91 and ZE41 in bicarbonate buffered Hanks' solution. *Corros. Sci.* **2015**, *101*, 182–192. [CrossRef]
37. Dong, Q.S.; Jia, Y.Q.; Ba, Z.X.; Tao, X.W.; Wang, Z.Z.; Xue, F.; Bai, J. Exploring the corrosion behavior of Mn-implanted biomedical Mg. *J. Alloys Compd.* **2021**, *873*, 159739. [CrossRef]
38. Cho, D.H.; Lee, B.W.; Park, J.Y.; Cho, K.M.; Park, I.M. Effect of Mn addition on corrosion properties of biodegradable Mg-4Zn-0.5Ca-xMn alloys. *J. Alloys Compd.* **2017**, *695*, 1166–1174. [CrossRef]
39. Song, G.; Atrens, A.; Stjohn, D.; Nairn, J.; Li, Y. The electrochemical corrosion of pure magnesium in 1N NaCl. *Corros. Sci.* **1997**, *39*, 855–875. [CrossRef]
40. Jin, S.; Zhang, D.; Lu, X.P.; Zhang, Y.; Tan, L.L.; Liu, Y.; Wang, Q. Mechanical properties, biodegradability and cytocompatibility of biodegradable Mg-Zn-Zr-Nd/Y alloys. *J. Mater. Sci. Technol.* **2020**, *47*, 190–201. [CrossRef]
41. Ba, Z.X.; Dong, Q.S.; Zhang, X.B.; Qiang, X.F.; Cai, Z.Y.; Luo, X. Cerium-based modification treatment of Mg-Al hydrotalcite film on AZ91D Mg alloy assisted with alternating electric field. *J. Alloys Compd.* **2017**, *695*, 106–113. [CrossRef]
42. Feng, Y.J.; Wei, J.; Chen, X.B.; Li, M.C.; Cheng, Y.F.; Li, Q. Unexpected cathodic role of Mg41Sm5 phase in mitigating localized corrosion of extruded Mg-Sm-Zn-Zr alloy in NaCl solution. *Corros. Sci.* **2019**, *159*, 108133. [CrossRef]
43. Wang, C.M.; Zeng, L.M.; Zhang, W.L.; Tang, F.Q.; Ding, W.C.; Xiao, S.F.; Liang, T.X. Enhanced mechanical properties and corrosion resistance of rolled Mg-1.5Sn-0.5Ca alloy by Ce microalloying. *Mater. Charact.* **2021**, *179*, 111325. [CrossRef]
44. Chen, H.; Tang, J.W.; Gong, W.W.; Gao, Y.P.; Tian, F.; Chen, L. Effects of annealing treatment on the microstructure and corrosion behavior of hot rolled AZ31 Mg alloy. *J. Mater. Res. Technol.* **2021**, *15*, 4800–4812. [CrossRef]
45. Kwon, J.; Baek, S.; Jung, H.; Kim, J.C.; Lee, S.; Park, S.S. Role of microalloyed Sm in enhancing the corrosion resistance of hot-rolled Mg–8Sn–1Al–1Zn alloy. *Corros. Sci.* **2021**, *185*, 109425. [CrossRef]
46. Cao, F.Y.; Zhang, J.; Li, K.K.; Song, C.L. Influence of heat treatment on corrosion behavior of hot rolled Mg5Gd alloys. *Trans. Nonferr. Met. Soc. China* **2021**, *31*, 939–951. [CrossRef]
47. Nene, S.S.; Kashyap, B.P.; Prabhu, N.; Estrin, Y.; Al-Samman, T. Microstructure refinement and its effect on specific strength and bio-corrosion resistance in ultralight Mg–4Li–1Ca (LC41) alloy by hot rolling. *J. Alloys Compd.* **2014**, *615*, 501–506. [CrossRef]